Original Paper

Non-artifact vector P- and S-wave separation for elastic reverse time migration

Xi-Yan Zhou [a, b, *], Xu Chang [c], Yi-Bo Wang [d], Xiao-Tao Wen [a, b], Jia-Chun You [a, b], Chang Sun [a, b]

[a] Key Laboratory of Earth Exploration and Information Techniques, Chengdu University of Technology, Chengdu, 610059, Sichuan, China
[b] College of Geophysics, Chengdu University of Technology, Chengdu, 610059, Sichuan, China
[c] Key Laboratory of Shale Gas and Geoengineering, Institute of Geology and Geophysics, Chinese Academy of Sciences, Beijing, 100029, China
[d] Key Laboratory of Petroleum Resource Research, Institute of Geology and Geophysics, Chinese Academy of Sciences, Beijing, 100029, China

ARTICLE INFO

ABSTRACT

Elastic reverse time migration (RTM) uses the elastic wave equation to extrapolate multicomponent seismic data to the subsurface and separate the elastic wavefield into P- and S-waves. P- and S-wave separation is a necessary step in elastic RTM to avoid crosstalk between coupled wavefields. However, the current curl-divergence operator-based separation method has a polarity reversal problem in PS imaging, and vector separation methods often have separation artifacts at the interface, which affects the quality of the imaging stack. We propose a non-artifact P- and S-wave separation method based on the first-order velocity-strain equation. This equation is used for wavefield extrapolation and separation in the first-order staggered-grid finite-difference scheme, and the storage and calculation amounts are consistent with the classical first-order velocity-stress equation. The separation equation does not calculate the partial derivatives of the elastic parameters, and thus, there is no artifact in the separated P- and S-waves. During wavefield extrapolation, the dynamic characteristics of the reflected wave undergo some changes, but the transmitted wavefield is accurate; therefore, it does not affect the dynamic characteristics of the final migration imaging. Through numerical examples of 2D simple models, part SEAM model, BP model, and 3D 4-layer model, different wavefield separation methods and corresponding elastic RTM imaging results are analyzed. We found that the velocity-strain based elastic RTM can image subsurface structures well, without spike artifacts caused by separation artifacts, and without polarity reversal phenomenon of the PS imaging.

1. Introduction

With the development of oil and gas exploration, exploration targets have become increasingly complex. To detect more comprehensive underground structures and lithological information, seismic exploration has gradually developed from conventional single-component acoustic exploration to three-dimensional multicomponent elastic wave exploration. Simultaneously, the advancement of multicomponent geophone technology has increased the application of multicomponent acquisition in oil and gas exploration. The multicomponent seismic acquisition can obtain sufficient seismic information and provide data support for underground converted shear-wave imaging. Shear waves have advantages in gas cloud area imaging, fracture prediction, fluid identification, and unconventional oil and gas exploration (Granli et al., 1999; Knapp et al., 2001; Stewart et al., 2003; Birt et al., 2020). Compared with single-component data, medium models have changed from acoustic to elastic models. In the processing and interpretation of multicomponent seismic data, elastic wave equations are required to accurately describe the kinematic and dynamic information of seismic waves.

Migration is a difficult and important problem in seismic data processing. The quality of the migrated profile determines the success or failure of the subsequent inversion and interpretation (Li and Qu, 2022). Current multicomponent seismic data migration is

mostly based on ray theory (Yang et al., 2015; Zhang et al., 2019). However, as exploration targets become increasingly complex, such as high-steep nappe structures, high-steep fault structures, and complex subsalt structures, the ray theory-based migration method has difficulty achieving precise imaging of complex structures. Elastic reverse time migration (RTM) can deal with any vertical and horizontal variable medium, can image complex structures, and can image multiples (Zhang et al., 2021; Zhao et al., 2021). Elastic RTM not only obtains traditional PP images, but also converted-wave PS images (Yan and Sava, 2008). The PP and PS images of the multi-component elastic RTM enrich the structural imaging information, provide support for P- and S-wave joint inversion and interpretation, and reduce the non-uniqueness of inversion and interpretation. Chang and McMechan (1987) proposed elastic RTM, which used the elastic wave equation to extrapolate multicomponent seismic data to the subsurface. However, the coupling of the P- and S-waves causes imaging crosstalk, and the imaging results have no clear physical meaning. Yan and Sava (2008) separated the P- and S-waves in wavefield extrapolation and then used the separated P- and S-wave cross-correlation imaging conditions to obtain high-precision PP and PS images of the subsurface structure, which can avoid crosstalk between the coupled wavefields. Therefore, P- and S-wave separation is a necessary step in elastic RTM. Furthermore, P- and S-wave separation is also the main step for elastic wavefield extrapolation-based processing and interpretation methods, such as seismic wavefield simulation, elastic reverse time imaging for source locating or converted-wave imaging (Shabelansky et al., 2015; Li et al. 2018, 2021; Du et al., 2019; Yang and Zhu, 2019; Lin et al., 2020; Zou and Cheng, 2021), elastic least-squares RTM (Li et al., 2017; Qu et al. 2018, 2019a, 2019b; Zhong et al., 2021; Wu et al., 2022), and elastic full waveform inversion (Wang and Cheng, 2015; Wang et al., 2018; Yao et al., 2020; Zhang et al., 2022).

Elastic P- and S-wave separation methods include curl-divergence operator separation and wavefield decoupling separation. The curl-divergence operator separates the P- and S-waves according to the difference between their propagation and vibration directions. The P-wave vibrates along the propagation direction and is a non-curling field, which is obtained by the divergence operator. The S-wave vibrates perpendicular to the propagation direction and is a non-divergence field, which is calculated by the curl operator. However, the curl and divergence operators are spatial difference operators that change the phase and amplitude of the separated wavefield (Sun et al. 2001, 2011). In addition, the P-wave separated by the divergence operator is a scalar. The S-wave separated by the curl operator is a scalar in a 2D medium, and the separated wavefield has polarity reversal in different propagation directions, which affects the multi-shot stack quality of the PS image in elastic RTM (Duan and Sava, 2015). In 3D, the S-wave separated by the curl operator is a vector; therefore, scalar PS imaging of elastic RTM is difficult (Du et al., 2014). The Helmholtz-based P- and S-wave separation methods can preserve the physical meaning, phase, and amplitude information of the decomposed wavefield, but this method requires to perform the 2D or 3D integral for each grid point, which is computationally intensive. Zhu (2017) introduced a fast Poisson solver to reduce computational complexity; however, this method is still computationally expensive. Based on Helmholtz's theory, Yang et al. (2018) changed the phase and amplitude of source wavelets and multicomponent records to achieve phase- and amplitude-preserving vector P- and S-wave separation. However, in sharp velocity contrasts, this method produces separation artifacts.

In recent years, wavefield decoupling-based P- and S-wave separation methods have been commonly used in elastic RTM (Zhang et al. 2007, 2020; Xiao and Leaney, 2010; Wang and McMechan, 2015; Elita Li et al., 2018; Zhou et al. 2018, 2019; Hu et al., 2019; Shi et al., 2019; Zhang and Shi, 2019; Qu et al., 2020; Li et al., 2021; Yang et al., 2021). The P- and S-waves separated by this method are all vectors, which maintains the dynamic information of the separated wavefield, such as phase and amplitude, and the physical meaning of the separated wavefield is consistent with the original wavefield. However, the derivation of the decoupling equation is based on the assumption of constant Lamé coefficient λ and μ; thus, separation artifacts exist at the subsurface interface (Tang and McMechan, 2018). For elastic RTM, the reflectivity at the interface is the imaging target; therefore, the P- and S-wave separation artifacts at the interface significantly affect the imaging quality. With this problem, Tang and McMechan (2018) proposed an improved system of P and S-wave separation that considers the converted wave generated at the current time, and it does not require the constant-shear-modulus assumption. Li et al. (2018) proposed second-order P- and S-potentials equations for P- and S-wave propagation without the assumption of homogeneous Lamé parameters. Du et al. (2020) proposed an equation without wavefield conversion at a discontinuous shear modulus for elastic RTM. Another method to reduce the separation artifacts is to smooth the migration velocity model so that μ changes slowly (Wang and McMechan, 2015; Yang et al., 2018). However, this method increases the limitations. When the velocities contain strong contrasts, excessive smoothing of the velocity model will affect the kinematic and dynamic characteristics of the wavefield, and insufficient smoothing will still cause separation artifacts.

This paper focuses on the P- and S-wave decoupling methods, and proposes first-order velocity-strain equation-based P- and S-wave decoupling methods. This method maintains the dynamic information of the separated wavefield, such as the amplitude and phase, and reduces separation artifacts. In this paper, we first analyzes the characteristics of the curl-divergence operator separation and first-order velocity-stress wavefield decoupling methods. In addition, we propose the first-order velocity-strain P- and S-wave separation method, and use this separation method in elastic RTM. Finally, we verify the effectiveness of this method using simple and complex numerical models.

2. Methods

Two conventional P- and S-wave separation methods are reviewed in this section, the curl-divergence operator-based separation method and the first-order velocity-stress equations-based wavefield decoupling method. The advantages and disadvantages of the two methods are analyzed. Aiming at the shortcomings of traditional methods, a non-artifact P- and S-wave decoupling method based on first-order velocity-strain equations is proposed.

2.1. Curl-divergence operator and Helmholtz-based P- and S-wave separation and characteristic analysis

The curl-divergence separation method is based on the Helmholtz theory to separate P- and S-waves (Yan and Xie, 2012; Sun et al., 2004; Dellinger and Etgen, 1990). This method assumes that the wavefield consists of the gradient of a non-curling field and the curl of a non-divergence field. The non-curling field is a potential function of the P-wave, and the non-divergence field is a potential function of the S-wave. Therefore, the S-wave is separated by the curl operator, and the P-wave is separated by the divergence operator of the original wavefield (Morse and Feshbach, 1954),

$$u_P = \nabla \cdot \boldsymbol{u},$$

$$\boldsymbol{u}_S = \nabla \times \boldsymbol{u}, \tag{1}$$

where $\boldsymbol{u}$ is the original vector wavefield, u_P is the separated scalar P-wave, $\boldsymbol{u}_S$ is the separated vector S-wave, $\nabla\cdot$ is the divergence operator, and $\nabla\times$ is the curl operator. In this method, the physical meaning of the separated wavefield is inconsistent with the original wavefield because of curl and divergence calculations. If the original input wavefield is a displacement field, then the separated wavefield after the curl and divergence calculations is the particle velocity field. The transformation of Equation (1) from the time-space domain to the frequency-wavenumber domain yields,

$$\tilde{u}_P = i\boldsymbol{k}\cdot\tilde{\boldsymbol{u}},$$

$$\tilde{\boldsymbol{u}}_S = i\boldsymbol{k}\times\tilde{\boldsymbol{u}}, \tag{2}$$

where $\tilde{\boldsymbol{u}}$, $\tilde{u}_p$, and $\tilde{\boldsymbol{u}}_s$ are the original vector wavefield, separated P-wave, and separated S-wave in the frequency-wavenumber domain, respectively; i is the imaginary unit; and $\boldsymbol{k}$ is the wavenumber vector. From Equation (2), this method will change the phase by 90° when multiplying the imaginary unit i, and will change the amplitude when multiplying the wavenumber vector $\boldsymbol{k}$. The P-wave is a scalar because it is the dot product of two vectors. The S-wave obtained by the curl operator in 2D (x-z plane) is a vector parallel to the y-axis, which can be regarded as a scalar. In 3D, the S-wave obtained by the curl operator is a vector.

To analyze the effect of P- and S-wave separation, we constructed a horizontal and vertical layer model, as shown in Fig. 1, where the horizontal layer is located at $z = 3$ km, and the vertical layer is located at $x = 3$ km. The size of this model is 4 km × 4 km, the interval is 10 m × 10 m, and the number of grid points is 400 × 400. The explosion source is a 10 Hz Ricker wavelet in the model (1.5 km, 1.5 km), and the source is added in particle velocity component. The time sampling interval is 1 ms. The separated P- and S-waves obtained by the curl-divergence separation method are shown in Fig. 2. We find that the P- and S-waves are clearly separated, but the separated S-waves exhibit a polarity reversal phenomenon.

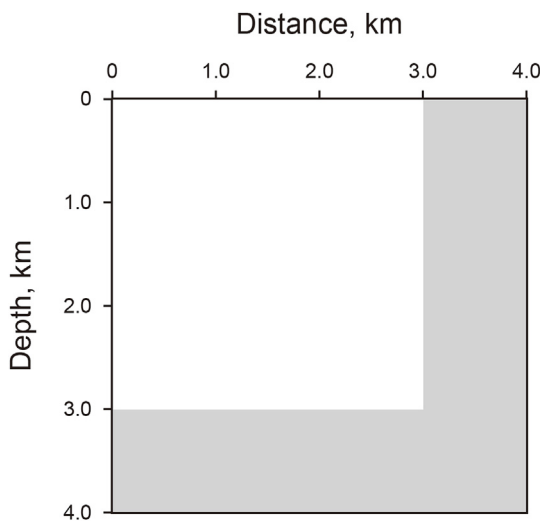At the same time, this method can further obtain the vector

separated wavefield based on the Helmholtz theory (Zhao et al., 2018),

$$\boldsymbol{u}_P = \nabla\left(\frac{\lambda + 2\mu}{\rho}\nabla\cdot\boldsymbol{u}\right),$$

$$\boldsymbol{u}_S = -\nabla\times\left(\frac{\mu}{\rho}\nabla\times\boldsymbol{u}\right), \tag{3}$$

where ρ, λ, and μ are the density and Lamé parameters. The method is to multiply the velocity term on the original curl and divergence operators, and then calculate the gradient and curl operations. To recover the true amplitude, the input source wavelet and the multicomponent records must be filtered by $\frac{1}{\omega^2}$, where ω is the angular frequency. The P- and S-waves separated by this method are vector field, and the phase and amplitude of the separated wavefield are consistent with the original wavefield. The P- and S-wave separation results obtained using the Helmholtz method are shown in Fig. 3. It is found that the separated P- and S-waves have separation artifacts at the interface.

2.2. Conventional first-order velocity-stress equation-based P- and S-wave decoupling method and artifact analysis

In recent years, the first-order velocity-stress equation-based wavefield decoupling method has been commonly used in elastic RTM for P-and S-wave separation. Based on the elastic first-order velocity-stress equations (Virieux, 1986; Graves, 1996),

$$\dot{v}_i = \frac{1}{\rho}\sigma_{ij,j}, \tag{4}$$

$$\dot{\sigma}_{ij,j} = \lambda\delta_{ij,j}v_{k,k} + \mu(v_{i,j} + v_{j,i}), \tag{5}$$

where v_i is the particle-velocity vector wavefield, and σ_{ij} is the stress. As shown in Appendix A, we can derive the velocity and stress relations from the basic equations of dynamic elasticity,

$$\frac{\partial v_x}{\partial t} = \frac{1}{\rho}\left\{\frac{\partial}{\partial x}\left[\frac{\lambda+2\mu}{2\lambda+2\mu}(\sigma_{xx}+\sigma_{zz})\right] + \frac{\partial\sigma_{xz}}{\partial z} - \frac{\partial}{\partial x}\left[\frac{(\lambda+2\mu)\sigma_{zz}-\lambda\sigma_{xx}}{2\lambda+2\mu}\right]\right\},$$

$$\frac{\partial v_z}{\partial t} = \frac{1}{\rho}\left\{\frac{\partial}{\partial z}\left[\frac{\lambda+2\mu}{2\lambda+2\mu}(\sigma_{xx}+\sigma_{zz})\right] + \frac{\partial\sigma_{xz}}{\partial x} - \frac{\partial}{\partial z}\left[\frac{(\lambda+2\mu)\sigma_{xx}-\lambda\sigma_{zz}}{2\lambda+2\mu}\right]\right\}, \tag{6}$$

If the medium is homogeneous, then the elastic parameters are constants; therefore, the partial derivatives of the elastic parameters λ and μ in the x- and z-directions are zero. The first term is the partial derivative of the normal stress, which is the P-wave term, and the second and third terms are the S-wave term. Therefore, the particle velocity term in the 2D medium is divided into P- and the S-waves (Zhang et al., 2007) as follows,

$$\dot{v}_{pi} = \frac{\lambda+2\mu}{\rho(2\lambda+2\mu)}(\sigma_{xx}+\sigma_{zz})_{,i}, \tag{7}$$

$$\dot{v}_{si} = \frac{\mu}{\rho}\left(\frac{1}{\mu}\sigma_{ij,j} - \frac{\lambda+2\mu}{\mu(2\lambda+2\mu)}\sigma_{kk,i}\right). \tag{8}$$

In addition, the separated P- and S-waves in 3D are (Zhou et al., 2018)

Fig. 1. Horizontal and vertical layers model. The model contains a vertical interface and a horizontal interface to observe the effect of P- and S-wave separation. The velocity model of the white part is ($v_P = 3,000$ m/s, $v_S = 1,800$ m/s, $\rho = 1,800$ kg/m³), and the gray part is filled as ($v_P = 3,500$ m/s, $v_S = 2,000$ m/s, $\rho = 2,000$ kg/m³).
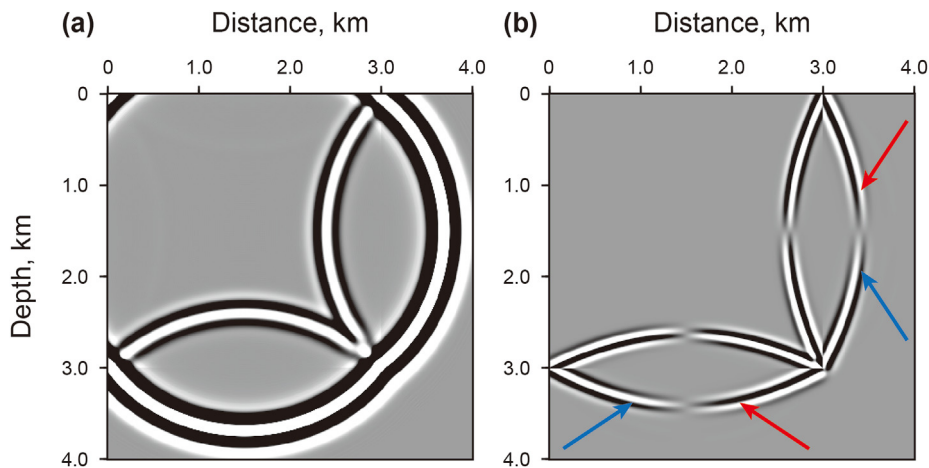
Fig. 2. Separated scalar P- and S-wave based on the curl-divergence separation method. (a) separated P-wave by the divergence operator; (b) separated S-wave by the curl operator, the red and blue arrows represent polarity reversal.
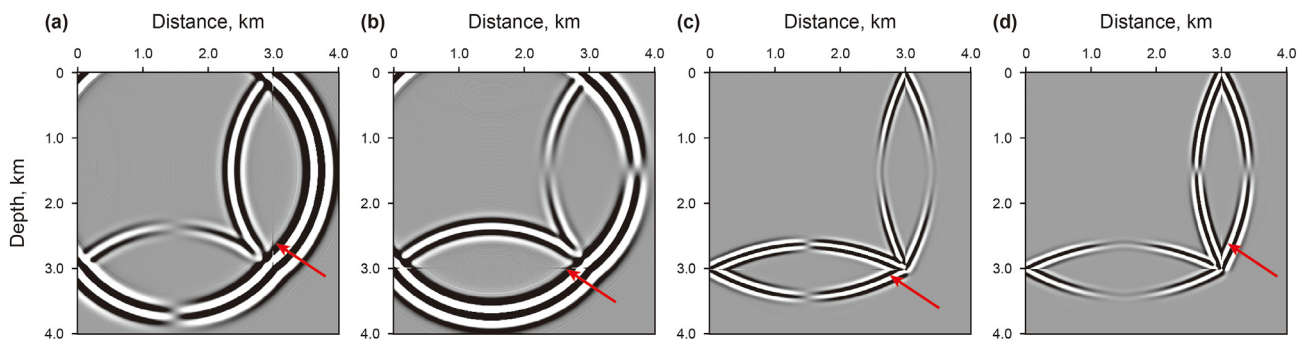

Fig. 3. Separated vector P- and S-wave based on Helmholtz separation. (a) and (b) separated x- and z-component of P-wave; (c) and (d) separated x- and z-component of S-wave. There is a thin line at the position of the red arrow, which is the separation artifacts.

$$\dot{v}_{pi} = \frac{\lambda+2\mu}{\rho(3\lambda+2\mu)}(\sigma_{xx}+\sigma_{yy}+\sigma_{zz})_{,i}, \tag{9}$$

$$\dot{v}_{si} = \frac{\mu}{\rho}\left(\frac{1}{\mu}\sigma_{ij,j} - \frac{\lambda+2\mu}{\mu(3\lambda+2\mu)}\sigma_{kk,i}\right), \tag{10}$$

where v_i, v_{pi}, and v_{si} are the original, separated P-wave, and separated S-wave particle-velocity vector wavefields, and σ_{ij} is the stress.

From the above derivation, it is clear that the first-order velocity-stress-based P- and S-wave decoupling equations are completely valid in homogeneous media. However, in inhomogeneous media, the elastic parameters are no longer constant, and the special derivative of the elastic parameters is not zero. The first-order velocity-stress P- and S-wave decoupling equations ignore the derivative term of the elastic parameters, so there is a high-energy separation artifact at the interface. From the inhomogeneous to homogeneous hypothesis, when the velocity model changes in the x-direction, the x-component P- and S-waves will have separation artifacts, and when the velocity model changes in the z-direction, the z-component P- and S-waves will have separation artifacts. In addition, we find that Equation (7) plus Equation (8) equals Equation (4), which indicates that the sum of the P- and S-wave terms is the total particle velocity, and the P- and S-wave artifacts are opposite to each other.

Similarly, we use the velocity model in Fig. 1 to simulate the wavefield and separate the P- and S-waves by decoupling the velocity-stress equation, the source is added in particle velocity component. The separated P- and S-waves are shown in Fig. 4. The separation results contain separation artifacts, and the different components have different characteristics. The separation artifacts of the P- and S-waves in the x-component are concentrated in the vertical layer, and the separation artifacts of the P- and S- wave in the z-components are concentrated in the horizontal layer. This phenomenon is consistent with the previous formula derivation hypothesis for the separation of P- and S-waves in the velocity-stress equation in the Section 2. Because the x-component omits the elastic parameter derivative in the x-direction, separation artifacts appear for the vertical layers. The z-component omits the derivative of the elastic parameters in the z-direction, so there will be separation artifacts in the horizontal layers. It is foreseeable that for the dipping stratum, there will be separation artifacts in the x- and z-components because the partial derivatives of the elastic parameters in the x- and z-directions are not zero. Because separation artifacts appear on the interface, which is the core of elastic RTM, the separation artifacts will cause incorrect migration imaging results.
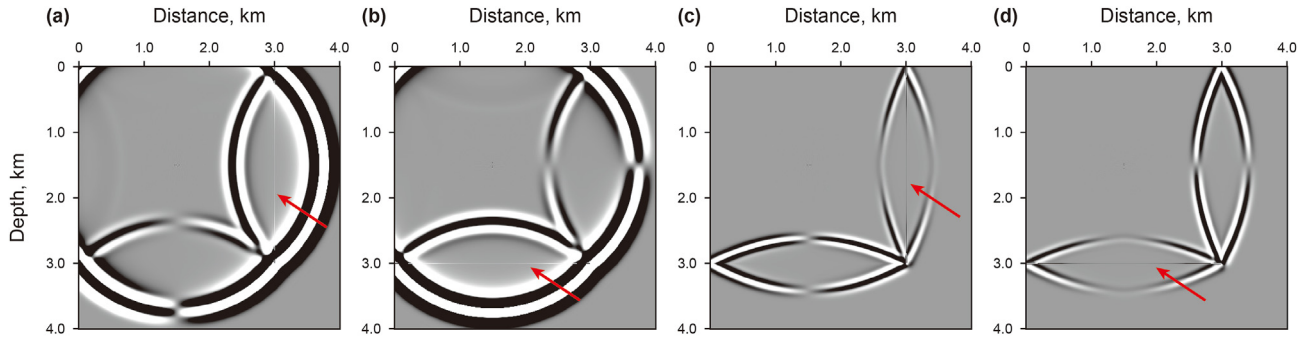
Fig. 4. Separated vector P- and S-wave based on velocity-stress equation. (a) and (b) separated x- and z-component of P-wave; (c) and (d) separated x- and z-component of S-wave. There is a thin line at the position of the red arrow, which indicates the separation artifacts.

2.3. Non-artifact P- and S-wave decoupling method based on the first-order velocity-strain equations

2.3.1. Decoupling equation based on the velocity-strain equations

We propose a P- and S-wave decoupling equation based on the first-order velocity-strain equation, which can realize the separation of P- and S-waves and avoid separation artifacts at the interface. The first-order velocity-strain equation is given by

$$\rho \dot{v}_i = \lambda \delta_{ij} \varepsilon_{kk,j} + 2\mu \varepsilon_{ij,j}, \tag{11}$$

$$\dot{\varepsilon}_{ij} = \frac{1}{2}\left(v_{i,j} + v_{j,i}\right). \tag{12}$$

Equation (12) does not require elastic parameters to obtain the strain term, and all the elastic parameters related terms are included the particle velocity calculation in Equation (11). In 2D, by extending the Einstein summation notation and organizing the equations into P- and S-wave velocity terms,

$$\dot{v}_x = \frac{\lambda + 2\mu}{\rho}\left(\varepsilon_{xx,x} + \varepsilon_{zz,x}\right) - \frac{2\mu}{\rho}\varepsilon_{zz,x} + \frac{2\mu}{\rho}\varepsilon_{xz,z},$$

$$\dot{v}_z = \frac{\lambda + 2\mu}{\rho}\left(\varepsilon_{xx,z} + \varepsilon_{zz,z}\right) - \frac{2\mu}{\rho}\varepsilon_{xx,z} + \frac{2\mu}{\rho}\varepsilon_{xz,x}, \tag{13}$$

The first term is the P-wave, and the last two terms are the S-wave. In a 2D medium, the corresponding P- and S-wave separation equations in the first-order velocity-strain equation are,

$$\dot{v}_{px} = \frac{\lambda + 2\mu}{\rho}\left(\varepsilon_{xx,x} + \varepsilon_{zz,x}\right),$$

$$\dot{v}_{pz} = \frac{\lambda + 2\mu}{\rho}\left(\varepsilon_{xx,z} + \varepsilon_{zz,z}\right), \tag{14}$$

$$\dot{v}_{sx} = -\frac{2\mu}{\rho}\varepsilon_{zz,x} + \frac{2\mu}{\rho}\varepsilon_{xz,z},$$

$$\dot{v}_{sz} = \frac{2\mu}{\rho}\varepsilon_{xz,x} - \frac{2\mu}{\rho}\varepsilon_{xx,z}.$$

Similarly, in a 3D medium,

$$\dot{v}_{px} = \frac{\lambda + 2\mu}{\rho}\left(\varepsilon_{xx,x} + \varepsilon_{yy,x} + \varepsilon_{zz,x}\right),$$

$$\dot{v}_{py} = \frac{\lambda + 2\mu}{\rho}\left(\varepsilon_{xx,y} + \varepsilon_{yy,y} + \varepsilon_{zz,z}\right),$$

$$\dot{v}_{pz} = \frac{\lambda + 2\mu}{\rho}\left(\varepsilon_{xx,z} + \varepsilon_{yy,z} + \varepsilon_{zz,z}\right), \tag{15}$$

$$\dot{v}_{sx} = -\frac{2\mu}{\rho}\left(\varepsilon_{yy,x} + \varepsilon_{zz,x}\right) + \frac{2\mu}{\rho}\left(\varepsilon_{xy,y} + \varepsilon_{xz,z}\right),$$

$$\dot{v}_{sy} = -\frac{2\mu}{\rho}\left(\varepsilon_{xx,y} + \varepsilon_{zz,y}\right) + \frac{2\mu}{\rho}\left(\varepsilon_{xy,x} + \varepsilon_{yz,z}\right),$$

$$\dot{v}_{sz} = -\frac{2\mu}{\rho}\left(\varepsilon_{xx,z} + \varepsilon_{yy,z}\right) + \frac{2\mu}{\rho}\left(\varepsilon_{xz,x} + \varepsilon_{yz,y}\right).$$

Therefore, the first-order velocity-strain equation-based P- and S-wave decoupling equations in 2D and 3D media are expressed in Einstein summation notation as

$$\dot{v}_{pi} = \frac{\lambda + 2\mu}{\rho}\varepsilon_{kk,i},$$

$$\dot{v}_{si} = -\frac{2\mu}{\rho}\varepsilon_{kk,i} + \frac{2\mu}{\rho}\varepsilon_{ij,j}. \tag{16}$$

Compared to Equation (6), Equation (13) does not calculate the partial derivatives of the elastic parameters. Therefore, the decoupling equation of the velocity-stress has a separation artifact, whereas the decoupling equation of the velocity-strain is precise. The velocity-strain based decoupling equation need not to omit the partial derivative of the Lamé coefficient. Therefore, the separated P- and S-waves can obtain accurate separation results that preserve the amplitude and phase information without separation artifacts.

2.3.2. Staggered-grid finite-differences scheme of the velocity-strain equations

The velocity-strain equation and the velocity-stress equation have similar expressions, so conventional finite element, spectral element, pseudo-spectral, finite-difference, and other methods can be used for the numerical simulation of the velocity-strain equation. In this paper, we use the staggered-grid finite-difference method for the numerical simulations. Compared with the regular grid finite-difference method, the staggered-grid finite-difference method has the advantages of higher precision and lower dispersion (Virieux, 1986). The first-order velocity-strain staggered-grid finite-difference is shown in Fig. 5. The terms v_{px} and v_{sx} are at the v_x position. The terms v_{pz} and v_{sz} are at the v_z position. The
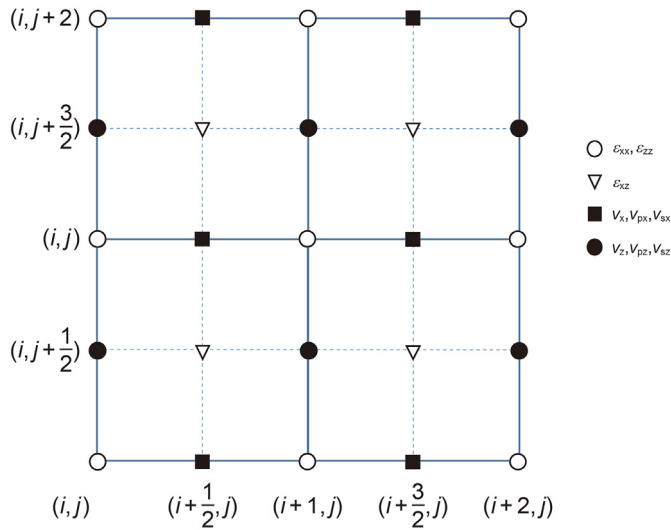
Fig. 5. Grid layout for the staggered-grid finite-differences scheme of the velocity-strain equation.

second-order in time and M-order in space staggered-grid finite-difference scheme of v_x can be expressed as,

$$
v_{x\ i+\frac{1}{2},j}^{n+\frac{1}{2}} = v_{x\ i+\frac{1}{2},j}^{n-\frac{1}{2}} + \frac{\Delta t}{\rho_{i+\frac{1}{2},j}} \sum_{m=1}^{M} C_m \lambda_{i+\frac{1}{2},j} \left[\varepsilon_{xx\ i+m,j}^{n} - \varepsilon_{xx\ i-m-1,j}^{n} + \varepsilon_{zz\ i,j+m}^{n} - \varepsilon_{zz\ i,j-m-1}^{n} \right]
$$

$$
+ \frac{\Delta t}{\rho_{i+\frac{1}{2},j}} \sum_{m=1}^{M} 2\mu_{i+\frac{1}{2},j} C_m \left[\varepsilon_{xz\ i,j+m}^{n} - \varepsilon_{xz\ i,j-m-1}^{n} \right],
$$

(17)

where i and j are the discrete coordinate positions in the x- and z-directions, and n is the time discrete coordinate. C_m is the staggered-grid finite-difference coefficient, which is obtained by Taylor expansion or by optimization methods such as least squares (Liu, 2014). The elastic parameters of the staggered position can be obtained by interpolation of the integer grid, such as $\rho_{i+\frac{1}{2},j}$, $\lambda_{i+\frac{1}{2},j}$, and $\mu_{i+\frac{1}{2},j}$ can be obtained by interpolation from $\rho_{i,j}$, $\lambda_{i,j}$, and $\mu_{i,j}$. The v_z term has a finite-difference scheme similar to v_x. The finite-difference scheme of ε_{xx} is expressed as,

$$
\varepsilon_{xx\ i,j}^{n} = \varepsilon_{xx\ i,j}^{n-1} + \frac{\Delta t}{\rho_{i,j}} \sum_{m=1}^{M} C_m \left[v_{x\ i-\frac{1}{2}+m,j}^{n-\frac{1}{2}} - v_{x\ i+\frac{1}{2}-m,j}^{n-\frac{1}{2}} + v_{z\ i,j-\frac{1}{2}+m}^{n-\frac{1}{2}} \right.
$$

$$
\left. - v_{z\ i,j+\frac{1}{2}-m}^{n-\frac{1}{2}} \right].
$$

(18)

Similarly, the terms ε_{zz} and ε_{xz} have a similar finite-difference scheme to ε_{xx}. The source can be added either in the particle velocity component or in the strain component. In this paper, the source is added in particle velocity component.

2.3.3. Comparison of separation effectiveness of velocity-stress and velocity-strain equations

To analyze the effectiveness of the P- and S-wave separation based on the velocity-strain equation, we use the staggered-grid finite-difference scheme of Equations (13) and (14) to simulate wavefield propagation for the velocity model shown in Fig. 1, and the explosion source of 10 Hz Ricker wavelet is added in particle velocity component. By Equation (16), the separated P- and S-wave based on the velocity-strain equation are shown in Fig. 6. It is found that the velocity-strain based decoupling equation can separate the P- and S-waves, and the separated P- and S-waves have no artifacts in either the horizontal or vertical layers. However, compared with Fig. 4, the reflected wave of the velocity-strain equation has a phase reversal relative to the velocity-stress equation. From the analysis in Appendix B, the velocity-stress equation corresponds to the second-order displacement equation in a heterogeneous medium, and the velocity-strain equation is equivalent to the second-order elastic wave equation in a homogeneous medium, so the velocity-strain equation is approximated in a heterogeneous medium. Fortunately, the velocity-strain equation can ensure the accuracy of the transmitted wavefield, and it can also ensure the accuracy of the source forward-propagated down-going wave and the receiver backward-propagated up-going wave in elastic RTM, so it can be used for the accurate imaging of elastic RTM. However, for the velocity-stress equation, the current vector separation methods, regardless of the P- and S-wave decoupling or the Helmholtz separation, have separation artifacts, which restrict their use in elastic RTM.

2.4. Elastic RTM based on non-artifact P- and S-wave decoupling

Elastic RTM is composed of wavefield extrapolation and imaging conditions. As shown in the flowchart in Fig. 7, we use Equations (11) and (12) to extrapolate the source forward wavefield and receiver inverse wavefield, respectively. Because the source wavefield propagates forward in time and the receiver wavefield propagates backward in time, and the source wavefield and receiver wavefield need to be multiplied at the same time in the imaging condition, elastic RTM has a massive memory demand. To reduce the source wavefield storage, we first calculate the source forward wavefield and then calculate the source backward wavefield by the boundary storage strategy (Clapp, 2008). Before the imaging condition, we separate the P- and S-waves of the source and receiver backward wavefield by Equation (14). Because the seismic source is mainly an explosion source in seismic exploration, we mainly consider PP and PS imaging. We choose the source P-wave and receiver P-wave to obtain the PP image, and choose the source P-wave and receiver S-wave to obtain the PS image. To maintain the image amplitude and phase accuracy, the imaging conditions of Zhou et al. (2019) are used here. The PP imaging condition is given by
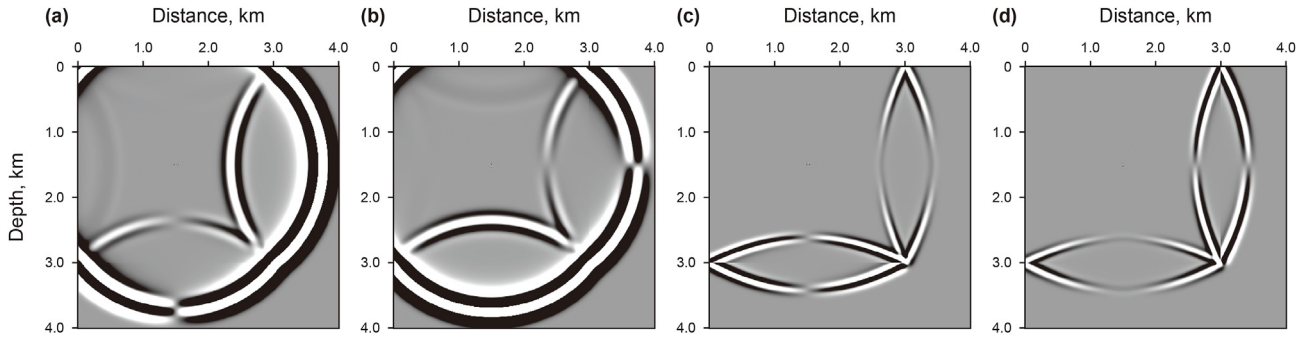
Fig. 6. Separated vector P- and S-wave based on velocity-strain equation. (a) and (b) separated x- and z-components of P-wave; (c) and (d) separated x- and z-components of S-wave.
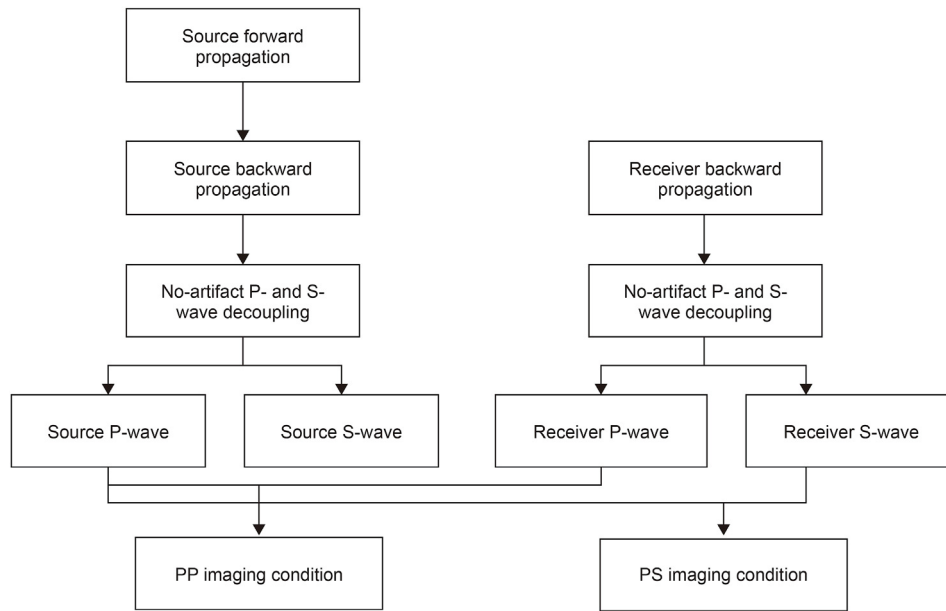

Fig. 7. Flowchart of single shot elastic RTM.

$$I_{PP}(x,y,z) = \frac{\sum_t \left(\overline{v}_p^{src}(x,y,z,t) \cdot \overline{v}_p^{rcv}(x,y,z,t) \right)}{\sum_t \left(\overline{v}_p^{src}(x,y,z,t) \cdot \overline{v}_p^{src}(x,y,z,t) \right)}, \quad (19)$$

$$\overline{v}_p = \sqrt{\frac{\lambda + 2\mu}{\rho}} \varepsilon_{kk}, \quad (20)$$

where $\overline{v}_p$ is the derived scalar P-wave (the specific derivation process are shown in Appendix), $\overline{v}_p^{src}(x,y,z,t)$ and $\overline{v}_p^{rcv}(x,y,z,t)$ are scalar P-waves from the extrapolation of the source and receiver wavefield, and $I_{PP}(x,y,z)$ is the PP imaging result.

It is difficult to derive amplitude and phase preserved scalar S-waves. Therefore, PS imaging can be divided into two parts: symbols and energy,

$$I_{PS}(x,y,z) = \frac{\sum_t sign_{PS} \cdot \left(\left| \boldsymbol{v}_p^{src}(x,y,z,t) \right| \cdot \left| \boldsymbol{v}_s^{rcv}(x,y,z,t) \right| \right)}{\sum_t \left(\overline{v}_p^{src}(x,y,z,t) \cdot \overline{v}_p^{src}(x,y,z,t) \right)}, \quad (21)$$

$$sign_{PS} = sign\left(\boldsymbol{v}_p^{src}(x,y,z,t) \cdot \boldsymbol{v}_s^{rcv}(x,y,z,t) \right), \quad (22)$$

where $\boldsymbol{v}_p^{src}(x,y,z,t)$ and $\boldsymbol{v}_s^{rcv}(x,y,z,t)$ are the source P-wave vector and receiver S-wave vector, respectively, $sign_{PS}$ is the PS imaging sign, and $I_{PS}(x,y,z)$ are the PS imaging results. This imaging condition can accurately describe amplitude preserved PS imaging without polarity reversal.

The main objective of elastic RTM is to image the PP and PS reflectivity of the subsurface interface, but the velocity-stress equation-based P- and S-wave separation will cause artifacts at the interface, which will affect reflectivity imaging. Therefore, we propose a non-artifact P- and S-wave vector decoupling method that can be used in elastic RTM. After amplitude preserving PP and PS imaging conditions, accurate PP and PS images can be obtained.

3. Numerical examples

3.1. Horizontal three-layer model

To analyze the impact of different P- and S-wave separation methods on elastic RTM, we constructed a simple three-layer velocity model, as shown in Fig. 8. The model has 600 grid points in
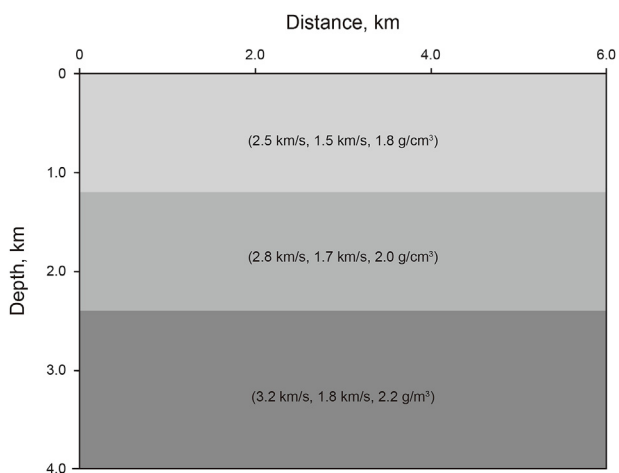
Fig. 8. Three-layer model. The parameters of P-wave velocity, S-wave velocity, and density of each layer are marked in parentheses.

the horizontal direction, and 400 grid points in the vertical direction, with an interval of 10 m × 10 m. We use the first-order velocity-stress equation to simulate the seismic gather of this model, with the time sampling being 1 ms, and the source is a 15 Hz Ricker wavelet. Next, with simulated seismic records as boundary

conditions, we use the true velocity model in Fig. 8 for migration. Velocity-stress equations and velocity-strain equations are used for wavefield extrapolation, P- and S-wave separation, and migration imaging. Figs. 9–12 show the PP and PS imaging results based on the curl-divergence separation method, Helmholtz separation method, wavefield decoupling method based on the velocity-stress equation, and wavefield decoupling method based on the velocity-strain equation, respectively. The PS image result based on the curl-divergence method exists polarity reversal, which will affect the PS multi-shot stack imaging quality. The PP and PS images based on the Helmholtz separation or wavefield decoupling methods have a horizontal line at the interface, as indicated by the red arrow, which is an imaging artifact; this is because of the separation artifacts. However, the imaging results obtained by the velocity-strain equation P- and S-wave separation methods have no artifacts at the interface and can effectively image the underground structure.

3.2. Complex model

To further verify the effect of P- and S-wave separation on elastic RTM, we use part of the SEAM model (Fehler and Larner, 2008) shown in Fig. 13 to compare and analyze the imaging results under different wavefield separation methods. This model is 7.5 km and 4 km in horizontal and vertical directions, respectively, and the space interval in both the x- and z-direction is 10 m. The model is composed of several reflective stratas, and there is salt in the lower-
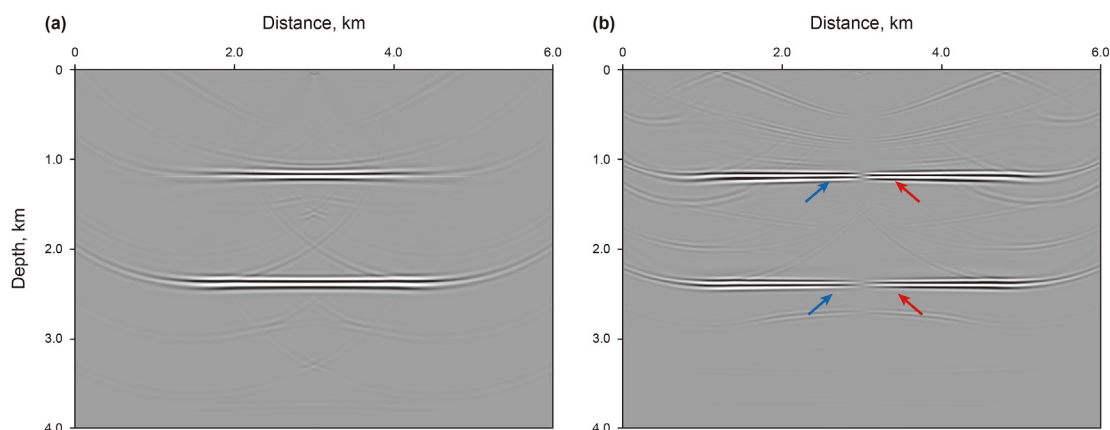

Fig. 9. (a) Elastic RTM PP imaging results and (b) elastic RTM PS imaging results obtained by the curl-divergence separation method of the three-layer model. There is a polarity reversal phenomenon in the PS image, shown by the red and blue arrows.
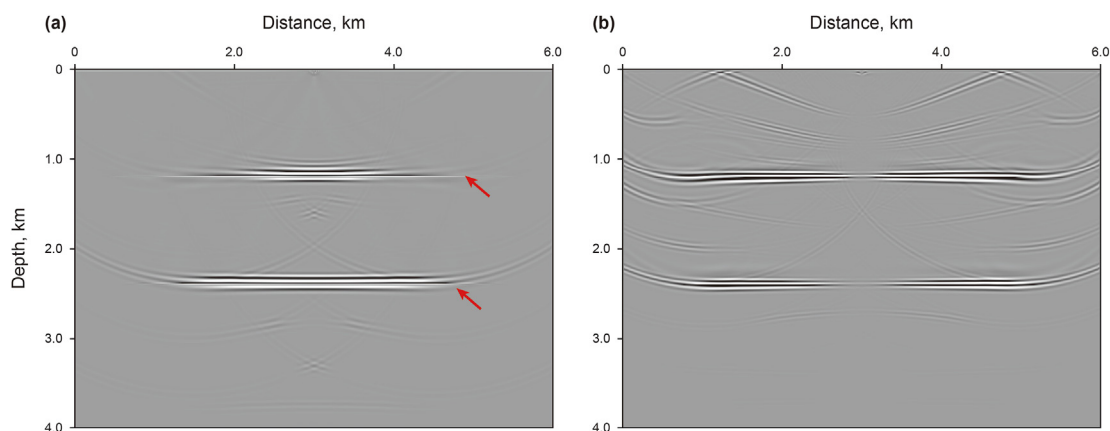

Fig. 10. (a) Elastic RTM PP imaging results and (b) elastic RTM PS imaging results obtained the Helmholtz separation method of the three-layer model. There are linear imaging artifacts in the PP image, which are indicated by red arrows.
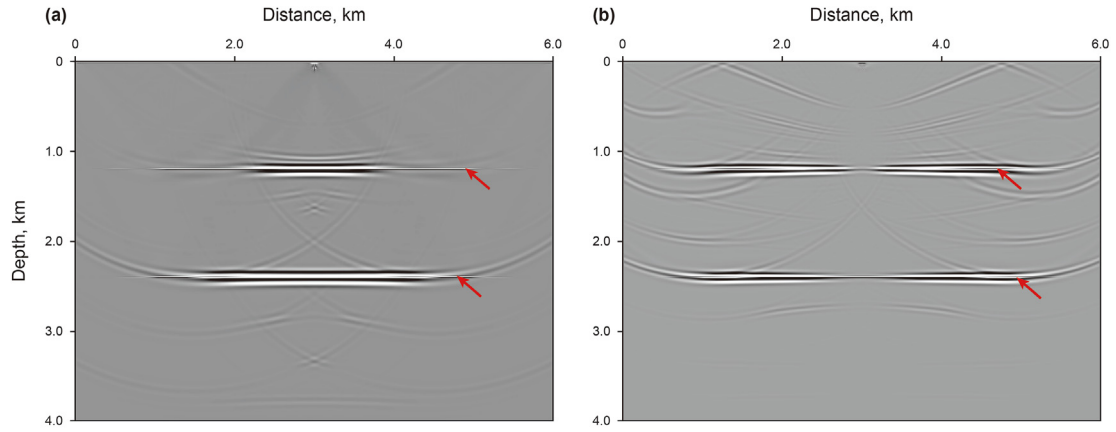
Fig. 11. (a) PP imaging results and (b) PS imaging results obtained by the velocity-stress equation-based P- and S-wave separation method of the three-layer model. There are linear imaging artifacts indicated by the red arrows.
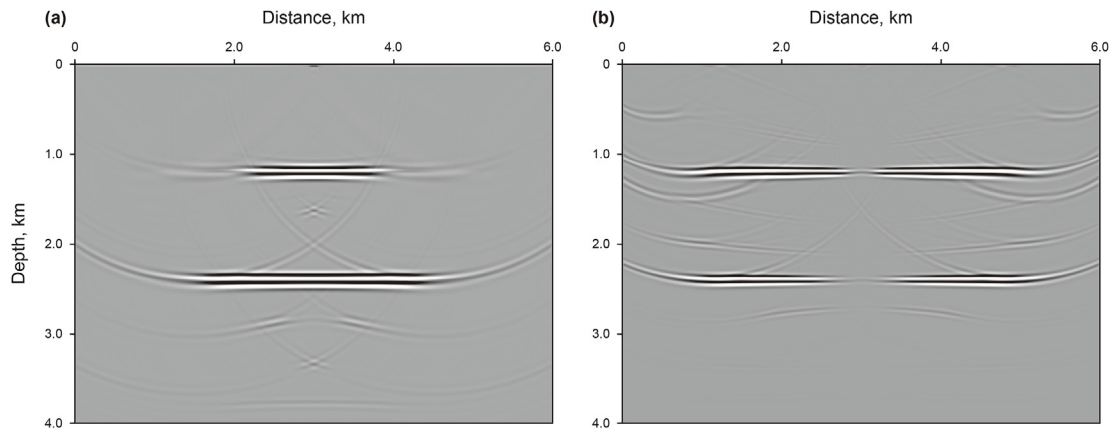

Fig. 12. (a) PP imaging result and (b) PS imaging result obtained by the velocity-strain equation-based P- and S-wave separation method of the three-layer model. These imaging results have no artifact.
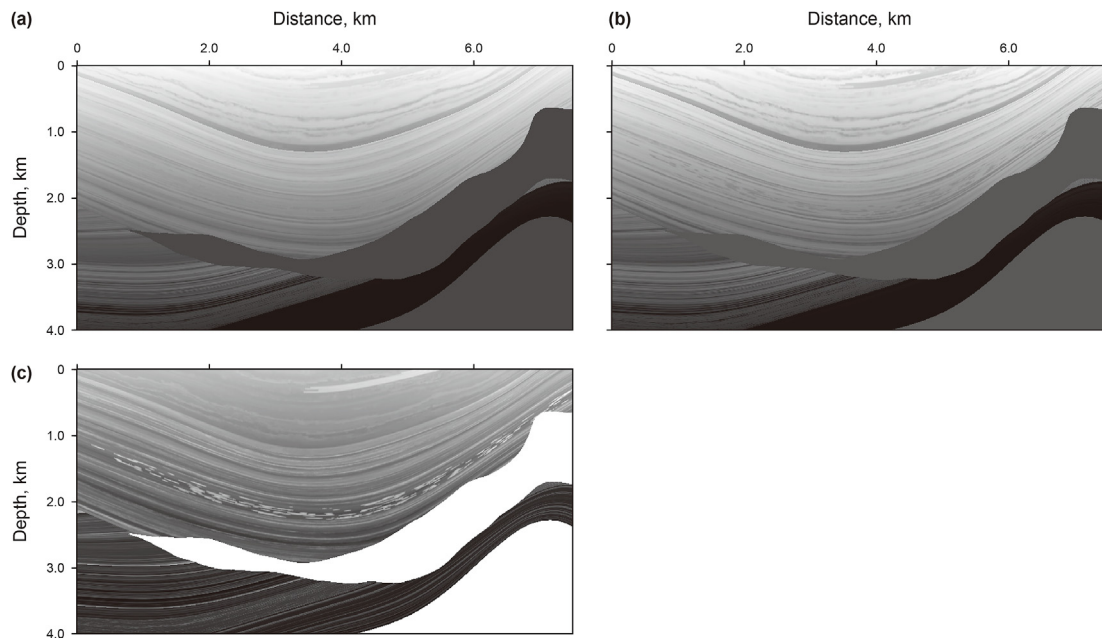

Fig. 13. (a) P-velocity, (b) S-velocity, and (c) density of the complex model.
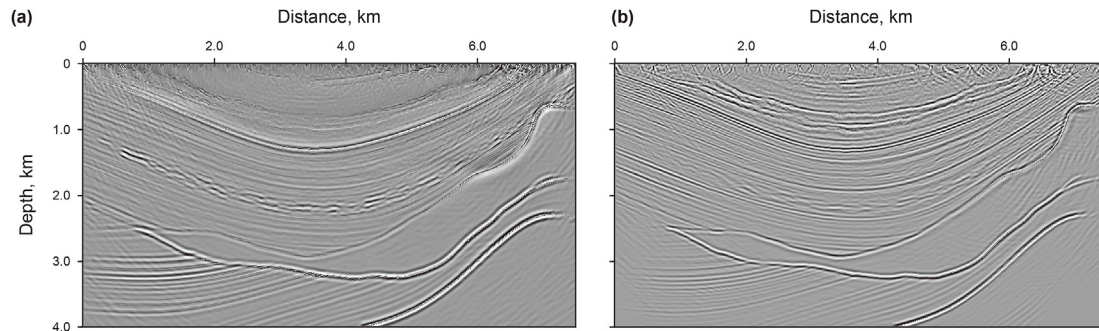
Fig. 14. (a) PP imaging result and (b) PS imaging result of the complex model obtained by the velocity-stress equation based P- and S-wave separation. The imaging event is not smooth, and it contains spikes and thin lines, which are migration artifacts.
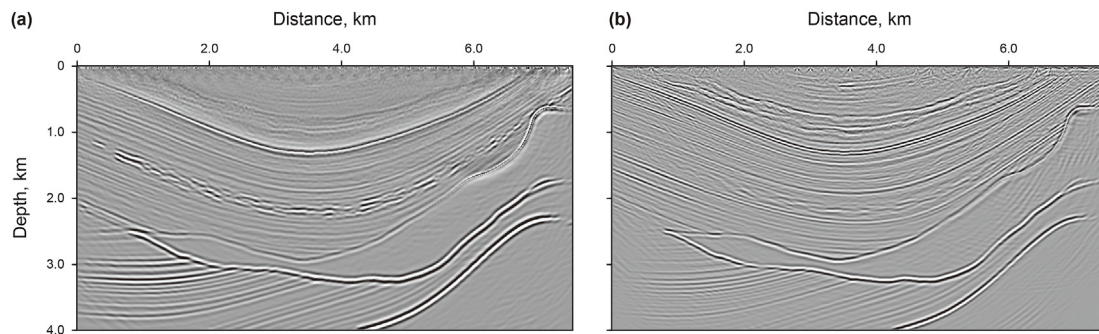

Fig. 15. (a) PP imaging result and (b) PS imaging result of the complex model obtained by the velocity-strain equation-based P- and S-wave separation. The imaging event is smoother than that in Fig. 14, and the imaging results have no imaging artifacts.

right part of the model. During the migration process, the source uses a Ricker wavelet with a dominant frequency of 15 Hz, and the time sampling is 1 ms. The PP and PS migration imaging results obtained by the velocity-stress equation-based P- and S-wave separation methods are shown in Fig. 14, and the PP and PS imaging results based on the velocity-strain equation are shown in Fig. 15. To show the imaging details of the two methods more clearly, we zoomed in the square area of 2.5–4 km in the *x*-direction and 2.5–4 km in the *z*-direction. The partial magnifications are shown in Fig. 16, where the upper part is the PP imaging result, the lower part is the PS imaging result, the left side is the imaging result obtained by the velocity-stress equation-based P- and S-wave separation, the middle part is the image obtained by the velocity-strain equation-based P- and S-wave separation, and on the right side is the difference between the imaging results of the velocity-stress and velocity-strain equations. The migration imaging results obtained by the velocity-stress equation-based P- and S-wave separation have obvious high-frequency imaging artifacts at the interface, while the imaging results obtained by the velocity-strain equation-based P- and S-wave separation can image the interface well, and without imaging artifacts. Through the imaging difference between the two imaging methods, it can be found that the imaging difference is mainly concentrated on these interfaces, the imaging results of the two methods are very remarkably close. This shows that the reflected wave phase reversal problem of the velocity-strain equation has little effect on the final elastic RTM imaging. Simultaneously, we also show the waveform of the PP and PS imaging results at 2, 4, and 6 km in Fig. 17. The imaging result curve obtained by the velocity-strain equation-based P- and S-wave separation is smooth. However, there are several spikes in the imaging results obtained by the velocity-stress equation-based P- and S-wave separation, and these spikes are migration imaging

artifacts caused by the separation artifacts. This example shows that the velocity-strain equation-based P- and S-wave separation methods and their elastic RTM are accurate, and there are no separation and imaging artifacts. Velocity-strain equation-based P- and S-wave separation methods is more suitable for elastic RTM than the velocity-stress equation-based P- and S-wave separation methods.

3.3. BP model

We also use the part of BP model (Billette and Brandsberg-Dahl, 2005) to verify the validity of the non-artifact P- and S-wave based elastic RTM. The BP model are shown in Fig. 18. This model is 2,301 and 856 grid points in horizontal and vertical directions, respectively, and the space interval in both the *x*- and *z*-direction is 12.5 m. The simulation source is Ricker wavelet with a dominant frequency of 10 Hz. To image the subsalt structure with the diving wave, we chose a large offset of 1,500 grid points for each shot. A total of 231 shots are evenly distributed on the surface of the model, and each shot is spaced by 10 grid points. The migration velocity model shown in Fig. 19 is obtained by smoothing the original model of Fig. 18. The migration model only slightly smooth the top interface of the salt dome, and the smoothing is more severe elsewhere. Because there is an obvious interface between the upper part of the salt dome and other strata, this marked layer can be easily determined by seismic profiles and logging data. Therefore, we assume that the specific location of the top of the salt dome is known, and the accurate velocity model in other places is not easy to obtain, so the smoothness is more serious in other places. By elastic RTM, the PP and PS migration results obtained by the velocity-stress equation-based P- and S-wave separation methods are shown in Fig. 20, and the PP and PS imaging results based on the velocity-strain
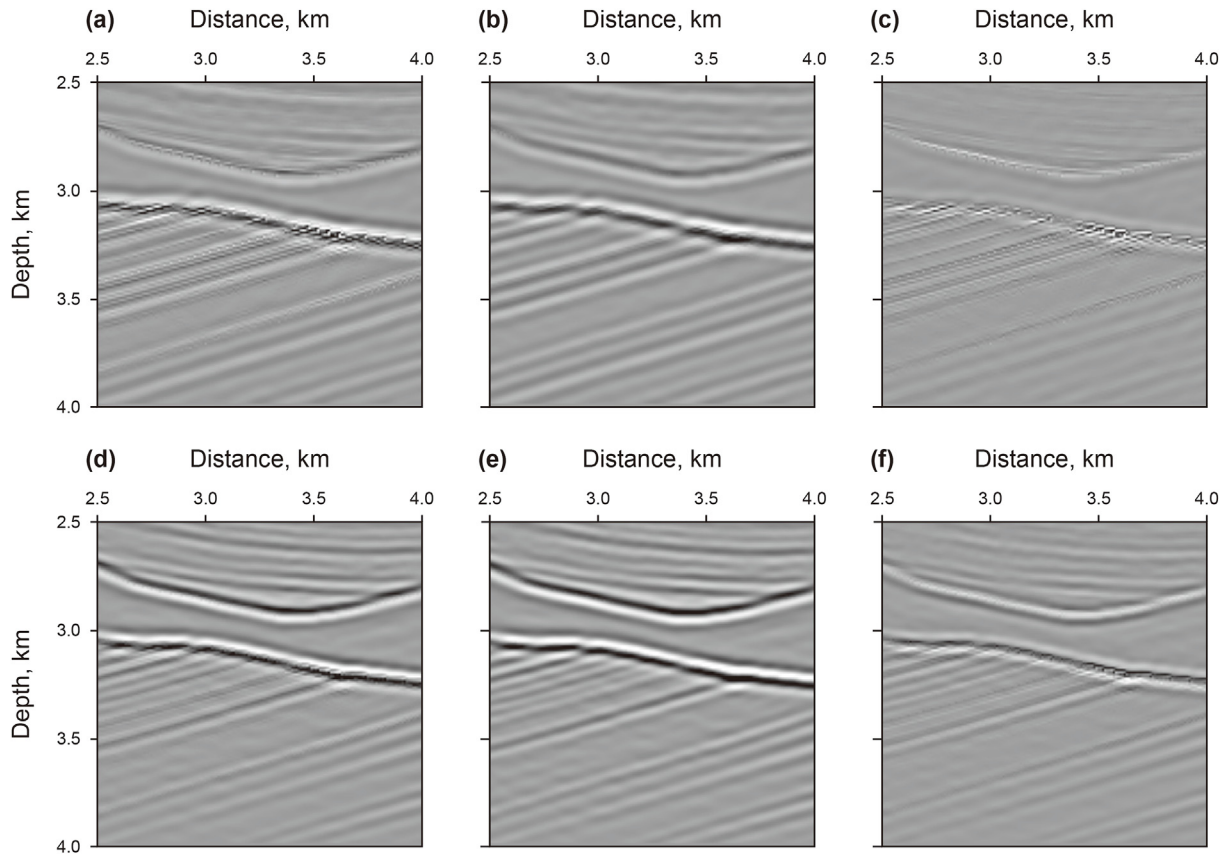
Fig. 16. Partial magnification of PP and PS images based on the velocity-stress equation, velocity-strain equation, and imaging differences in the square area of 2.5–4 km in the *x*-direction and 2.5–4 km in the *z*-direction of Figs. 14 and 15. (a) and (d) are the PP and PS imaging results obtained by the velocity-stress equation-based P- and S-wave separation, (b) and (e) are the PP and PS imaging results obtained by the velocity-strain equation-based P- and S-wave separation, (c) and (f) are the PP and PS image difference of velocity-stress and velocity-strain based imaging.
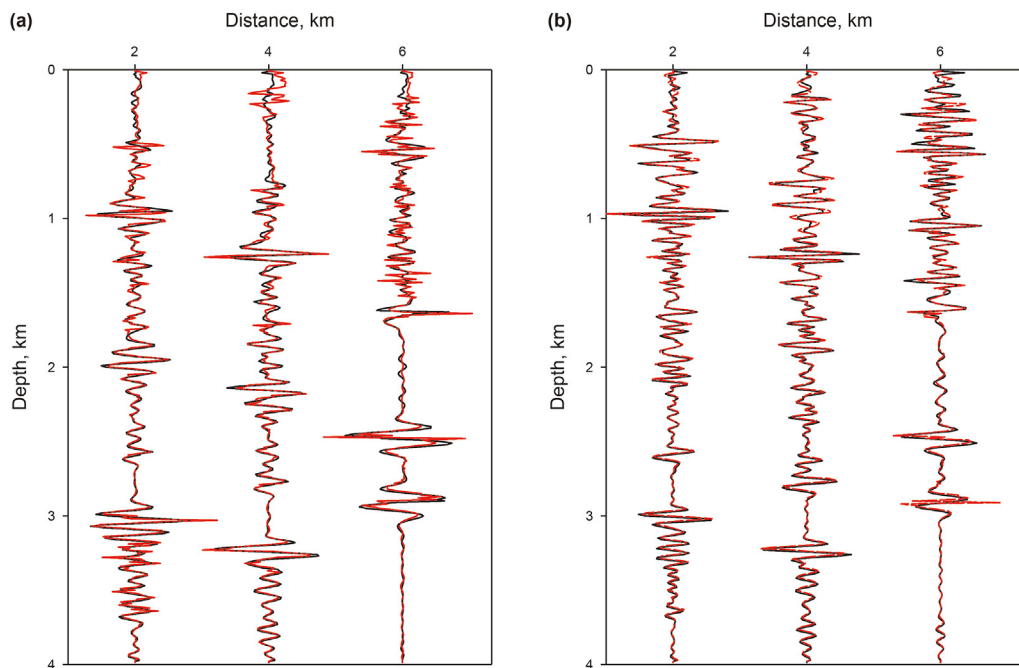

Fig. 17. Image curve comparison of velocity-stress based imaging result (red dotted line) and velocity-strain based imaging result (black line) at 2, 4 and 6 km in the *x*-direction. (a) PP imaging result curve comparison chart, (b) PS imaging result curve comparison chart.
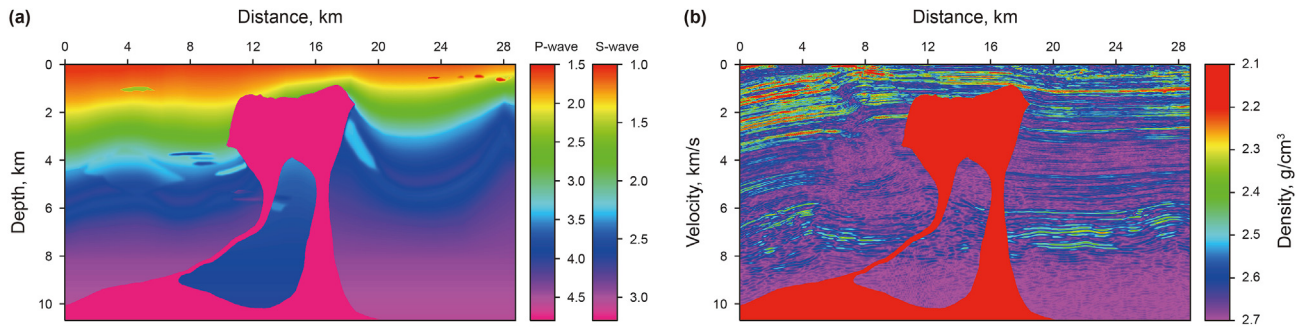
Fig. 18. Partial of BP model, (a) P- and S-wave velocity models, the color bars on the right represent P-wave and S-wave velocity values, respectively, (b) density model.
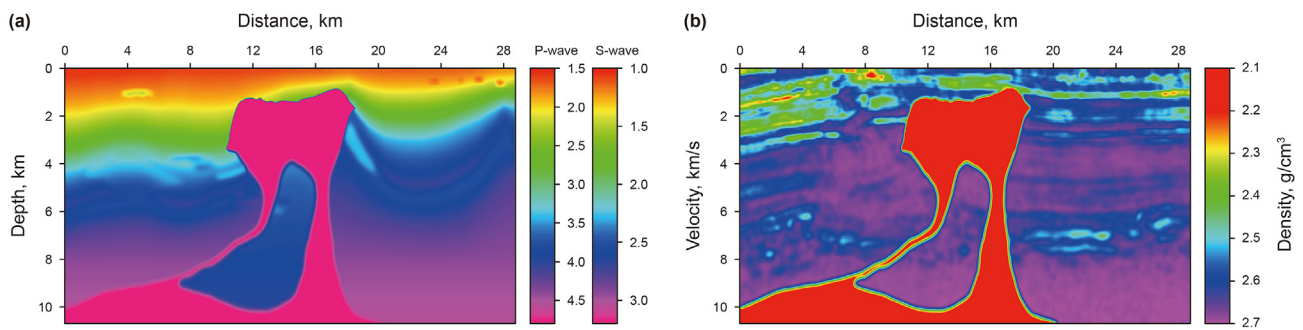

Fig. 19. Migration model, (a) P- and S-wave velocity models, (b) density model. The top of the salt dome is less smooth than elsewhere.

Fig. 20. (a) PP and (b) PS results of the BP model obtained by the velocity-stress equation-based elastic RMT. The lower right corner is a partial enlargement of the black box at the upper left of the salt dome.
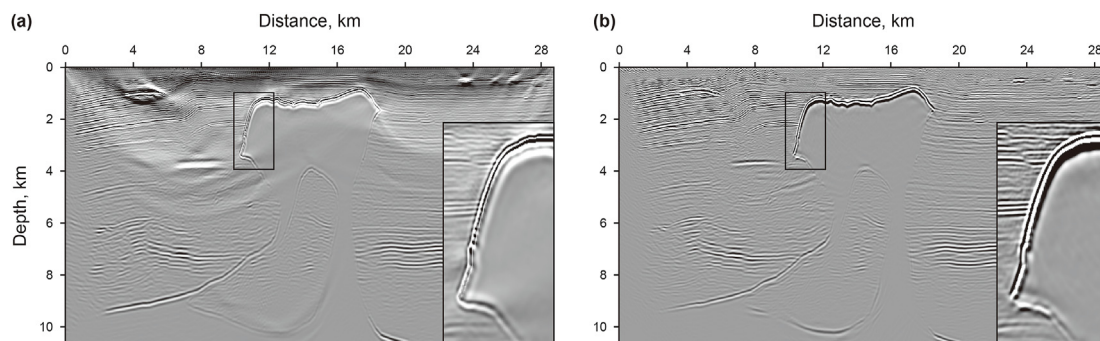

Fig. 21. (a) PP and (b) PS results of the BP model obtained by the velocity-strain equation-based non-artifact P- and S-wave separation. The lower right corner is a partial enlargement of the black box at the upper left of the salt dome.
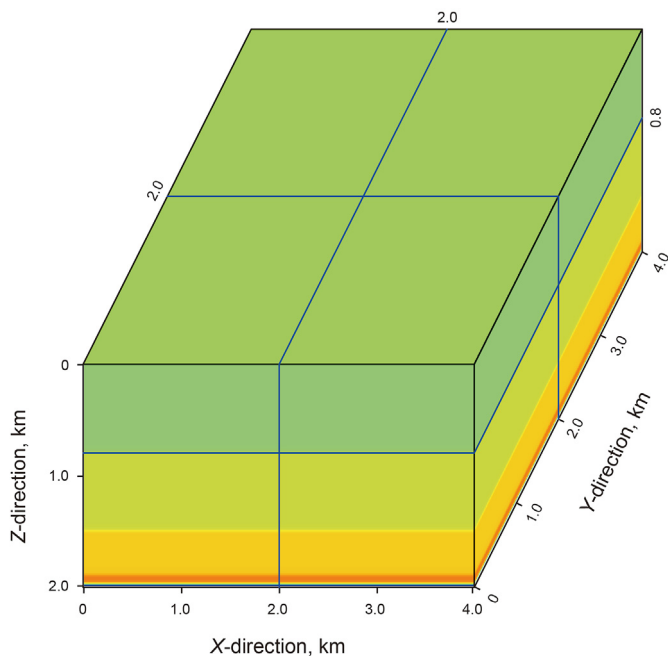
Fig. 22. 3D 4-layers model. The P-wave velocity, S-wave velocity, and density of this 4-layers model from top to bottom are (2,600 m/s, 1,200 m/s, 2.3 g/cm^3), (2,700 m/s, 1,300 m/s, 2.4 g/cm^3), (2,800 m/s, 1,400 m/s, 2.5 g/cm^3), (2,900 m/s, 1,500 m/s, 2.6 g/cm^3).

equation are shown in Fig. 21. It can be found that the two methods can accurately image the underground structure. Except for the top of the salt dome, the two imaging results are basically the same. However, the velocity-strain equation-based elastic RTM can better imaging the top of the salt dome than the velocity-stress equation, as shown in the partial enlargement of Figs. 20 and 21. Because the migration velocity model has a distinct interface at the top of the salt dome, the P- and S-wave separation artifact based on the velocity-stress equation can lead to artifacts in its elastic RTM imaging results. However, the elastic RTM based on the non-artifact P- and S-wave separation method proposed in this paper can better image the interface where the elastic parameters change rapidly.

3.4. 3D 4-layer model

We also built a simple 3D 4-layer model shown in Fig. 22 to test the validity of the non-artifact P- and S-wave separation based elastic RTM in 3D. This model is 400, 400, and 200 grid points in *x*-, *y*- and *z*-direction, and the space interval in both the *x*-, *y*-, and *z*-direction is 10 m. The source is 10 Hz Ricker wavelet. The PP and PS migration imaging results obtained by the velocity-stress equation-based P- and S-wave separation methods are shown in Fig. 23, and the PP and PS imaging results based on the velocity-strain equation are shown in Fig. 24. It can be found that the two methods can image the underground structure. However, there are several spikes in the imaging results of the velocity-stress equation-based elastic RTM, while the imaging results obtained by the velocity-strain equation-based elastic RTM can image the interface well, and without imaging artifacts.

4. Discussion

The non-artifact vector P- and S-wave separation equations proposed in this paper are an approximate equation. By comparing Figs. 6 and 4, it can be found that the transmitted wave is consistent with the first-order velocity-stress equation, and the reflected wave has a phase inversion problem. However, elastic RTM uses the transmitted wave of the source forward-propagated and receiver backward-propagated wavefields to calculate the cross-correlation imaging conditions, so this approximation has trivial effect on the imaging results of elastic RTM. From the migration imaging waveforms in Fig. 17, the amplitude and phase of the imaging results of the two methods are roughly the same, but the presence of spikes in the imaging results caused by separation artifacts will have a greater impact on the imaging quality. Therefore, we believe that non-artifact P- and S-wave separation methods are more suitable for elastic RTM. Simultaneously, we envision that the non-artifact P- and S-wave separation methods may also be suitable for the following situations:

(1) Elastic RTM with substantial changes in velocity

In elastic RTM, when the velocity model changes significantly, such as in the salt model, insufficient model smoothing may still cause separation artifacts, resulting in imaging spike artifacts and
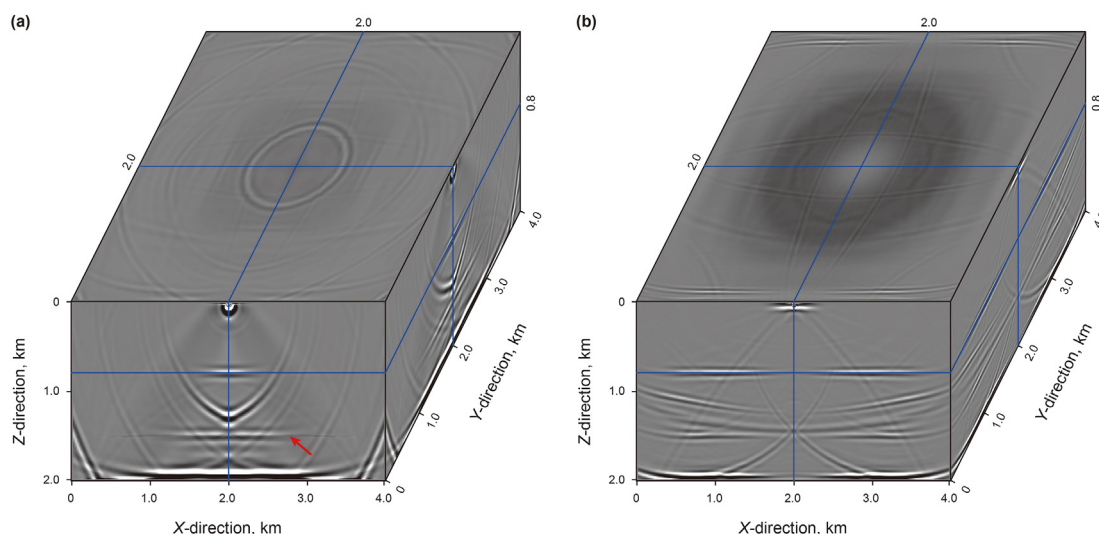

Fig. 23. (a) PP imaging result and (b) PS imaging result of the 3D model obtained by the velocity-stress equation-based P- and S-wave separation.
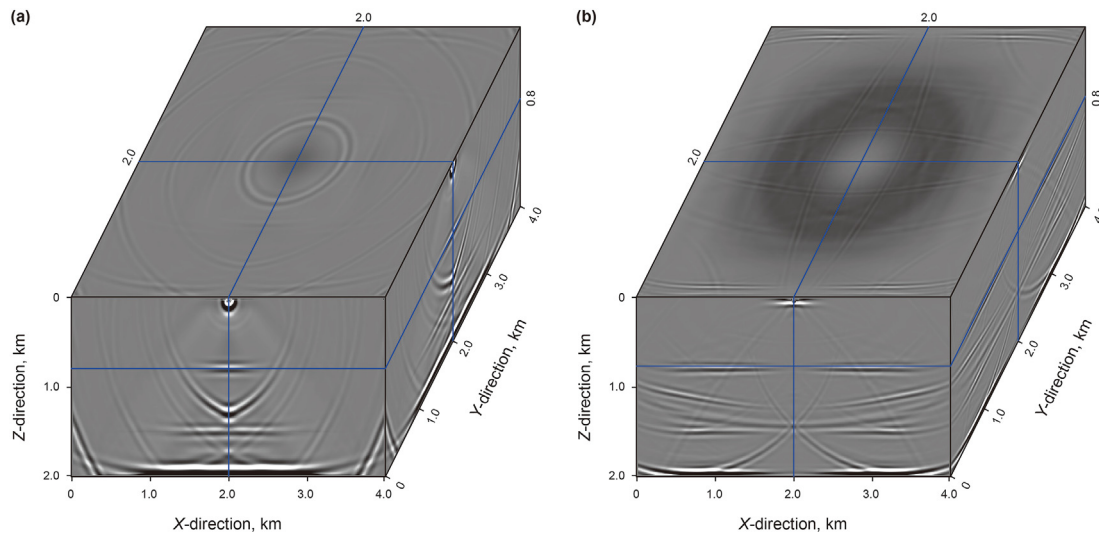
(a)

(b)

Fig. 24. (a) PP imaging result and (b) PS imaging result of the 3D model obtained by the velocity-strain equation-based P- and S-wave separation.

affecting later interpretation. However, excessive smoothing affects the kinematics and dynamic accuracy of the forward and backward wavefields and affects the final imaging quality. Therefore, for the elastic RTM of the model with severe velocity changes, the non-artifact P- and S-wave separation methods have great application prospects.

(2) Up/down separation imaging of the elastic RTM

To remove the low-frequency noise and velocity gradients caused false images, Fei et al. (2015) proposed up/down separation based RTM. If the up/down separation is used for elastic RTM, the P- and S-wave separation artifacts will cause obvious smearing in the up and down wavefields, which will affect the imaging quality. Therefore, it is also necessary to adopt non-artifact P- and S-wave separation methods in up/down separation based elastic RTM.

(3) Least squares elastic RTM or elastic full waveform inversion

With the increase in inversion iterations number of least squares elastic RTM or elastic full waveform inversion, the reflectivity model and the velocity model will become more and more accurate. An accurate reflection interface can easily lead to P- and S-wave separation artifacts at the interface, particularly at sharp interfaces or strong velocity contrasts. These artifacts affect the inversion quality. Therefore, it is also necessary to adopt non-artifact P- and S-wave separation in these methods.

5. Conclusions

The P- and S-wave separation methods are the basis of elastic RTM. However, the traditional curl-divergence operator-based separation method cannot maintain the dynamic characteristics of the separated wavefield, and the velocity-stress equation-based wavefield decoupling methods have separation artifacts. In this paper, we propose a velocity-strain equation-based P- and S-wave separation methods that maintain the dynamic characteristics of the separated wavefield, and there is no separation artifact in the separated wavefield. Used in elastic RTM, the velocity-strain based separation method can accurately separate the P- and S-wave in the extrapolated elastic wavefield and the imaging results obtained by the velocity-strain based separation method are smooth, with no migration artifacts.

Appendix A. Derivation of Equation (6)

The basic equations in dynamic elasticity consist of the motion equations,

$$\rho \ddot{u}_i = \sigma_{ij,j} + \rho f_i, \tag{A-1}$$

the strain-displacement relations,

$$\varepsilon_{ij} = \frac{1}{2}\left(u_{i,j} + u_{j,i}\right), \tag{A-2}$$

and the stress-strain relations in isotropic media,

$$\sigma_{ij} = \lambda \varepsilon_{kk}\delta_{ij} + 2\mu\varepsilon_{ij}, \tag{A-3}$$

where u_i is the displacement, and f_i is the body force (Aki and Richards, 2002). Equation (4) is derived from Equation (A-1) by omitting the body force and using the particle velocity instead of the displacement. Equation (5) is derived by substituting Equation (A-2) into Equation (A-3) and calculating the first-order partial derivation of time.

By substituting Equation (A-3) into Equation (A-1), the displacement-strain relations can be obtained,

$$\rho \ddot{u}_i = \left(\lambda \varepsilon_{kk}\delta_{ij} + 2\mu\varepsilon_{ij}\right)_{,j}. \tag{A-4}$$

By expanding the Einstein summation in 2D and calculating the first-order partial derivation of time, the particle velocity-strain relations can be obtained as follows,

$$\frac{\partial v_x}{\partial t} = \frac{1}{\rho}\left\{\frac{\partial}{\partial x}[\lambda(\varepsilon_{xx} + \varepsilon_{zz})] + \frac{\partial}{\partial z}(2\mu\varepsilon_{xz})\right\},$$

$$\frac{\partial v_z}{\partial t} = \frac{1}{\rho}\left\{\frac{\partial}{\partial z}[\lambda(\varepsilon_{xx} + \varepsilon_{zz})] + \frac{\partial}{\partial x}(2\mu\varepsilon_{xz})\right\}. \tag{A-5}$$

Recombining Equation (A-5) provides,

$$\frac{\partial v_x}{\partial t} = \frac{1}{\rho} \left\{ \frac{\partial}{\partial x} \left[(\lambda + 2\mu)(\varepsilon_{xx} + \varepsilon_{zz}) \right] + \frac{\partial}{\partial z} (2\mu\varepsilon_{xz}) - \frac{\partial}{\partial x} (2\mu\varepsilon_{zz}) \right\},$$

$$\frac{\partial v_z}{\partial t} = \frac{1}{\rho} \left\{ \frac{\partial}{\partial z} \left[(\lambda + 2\mu)(\varepsilon_{xx} + \varepsilon_{zz}) \right] + \frac{\partial}{\partial x} (2\mu\varepsilon_{xz}) - \frac{\partial}{\partial z} (2\mu\varepsilon_{xx}) \right\},$$
(A-6)

By substituting the strain and stress relationship into Equation (A-6) (Aki and Richards, 2002),

$$\varepsilon_{ij} = -\frac{\lambda}{2\mu(2\lambda + 2\mu)} \sigma_{kk}\delta_{ij} + \frac{1}{2\mu}\sigma_{ij}$$
(A-7)

the velocity and stress equation can be obtained,

$$\frac{\partial v_x}{\partial t} = \frac{1}{\rho} \left\{ \frac{\partial}{\partial x} \left[\frac{\lambda + 2\mu}{2\lambda + 2\mu} (\sigma_{xx} + \sigma_{zz}) \right] + \frac{\partial \sigma_{xz}}{\partial z} - \frac{\partial}{\partial x} \left[\frac{(\lambda + 2\mu)\sigma_{zz} - \lambda\sigma_{xx}}{2\lambda + 2\mu} \right] \right\},$$

$$\frac{\partial v_z}{\partial t} = \frac{1}{\rho} \left\{ \frac{\partial}{\partial z} \left[\frac{\lambda + 2\mu}{2\lambda + 2\mu} (\sigma_{xx} + \sigma_{zz}) \right] + \frac{\partial \sigma_{xz}}{\partial x} - \frac{\partial}{\partial z} \left[\frac{(\lambda + 2\mu)\sigma_{xx} - \lambda\sigma_{zz}}{2\lambda + 2\mu} \right] \right\},$$
(A-8)

which is Equation (6) in the Section 2.

Appendix B. Comparison of velocity-stress and velocity-strain equations

There are some differences in the wavefields obtained based on the first-order velocity-stress equation and first-order velocity-strain equation, mainly in terms of whether the equations calculate partial derivatives of the elastic parameters. By substituting stress Equation (5) into the velocity Equation (4) and replacing the velocity term with displacement, the second-order displacement equation corresponding to the velocity-stress equation is obtained as,

$$\rho \frac{\partial^2 u_x}{\partial t^2} = \frac{\partial}{\partial x} \left(\lambda \left(\frac{\partial u_x}{\partial x} + \frac{\partial u_z}{\partial z} \right) + 2\mu \frac{\partial u_x}{\partial x} \right) + \frac{\partial}{\partial z} \left(\mu \left(\frac{\partial u_z}{\partial x} + \frac{\partial u_x}{\partial z} \right) \right)$$

$$\rho \frac{\partial^2 u_z}{\partial t^2} = \frac{\partial}{\partial z} \left(\lambda \left(\frac{\partial u_x}{\partial x} + \frac{\partial u_z}{\partial z} \right) + 2\mu \frac{\partial u_z}{\partial z} \right) + \frac{\partial}{\partial x} \left(\mu \left(\frac{\partial u_z}{\partial x} + \frac{\partial u_x}{\partial z} \right) \right)$$
(B-1)

Because Equation (B-1) computes partial derivatives for the elastic parameters, the separation of the longitudinal and shear wavefields based on the decoupling equations of the velocity-stress equations creates an artifact at the interface.

Similarly, by substituting strain Equation (12) into velocity Equation (11), and replacing the velocity term with the displacement, the second-order displacement equation corresponding to the velocity-strain equation is obtained as,

$$\rho \frac{\partial^2 u_x}{\partial t^2} = (\lambda + 2\mu) \left(\frac{\partial^2 u_x}{\partial x^2} + \frac{\partial^2 u_z}{\partial x \partial z} \right) + \mu \left(\frac{\partial^2 u_x}{\partial z^2} + \frac{\partial^2 u_z}{\partial x \partial z} \right)$$

$$\rho \frac{\partial^2 u_z}{\partial t^2} = (\lambda + 2\mu) \left(\frac{\partial^2 u_z}{\partial z^2} + \frac{\partial^2 u_z}{\partial x \partial z} \right) + \mu \left(\frac{\partial^2 u_x}{\partial x^2} + \frac{\partial^2 u_x}{\partial x \partial z} \right)$$
(B-2)

Equation (B-2) does not calculate the partial derivatives for elastic parameters, so the corresponding decoupling equation does not have artifacts at the interface.

Appendix C. Derivation of scalar P-wave from the velocity-strain equation

In an isotropic medium, the P-wave vibration direction is parallel to the propagation direction, so the scalar P-wave is obtained by multiplying the vector P-wave by the P-wave propagation direction,

$$\bar{v}_p = \boldsymbol{v}_P \cdot \boldsymbol{n}_P,$$
(C-1)

where $\boldsymbol{v}_P$ is the vector P-wave, $\bar{v}_p$ is the scalar P-wave, and $\boldsymbol{n}_P$ is the P-wave normalized propagation direction. By substituting the P-wave decoupling formula of Equation (15) into Equation (C-1), we obtain,

$$\frac{\partial \bar{v}_p}{\partial t} = \frac{\lambda + 2\mu}{\rho} \left(\varepsilon_{kk,i} \cdot n_{Pi} \right).$$
(C-2)

This is Einstein's summation notation, and n_{Pi} is a component of $\boldsymbol{n}_P$. By transforming Equation (C-2) from the time-space domain to the frequency-wavenumber domain,

$$i\omega\bar{v}_p = \frac{\lambda + 2\mu}{\rho} (ik_x\widehat{\varepsilon}_{kk}, ik_z\widehat{\varepsilon}_{kk}) \cdot \widehat{\boldsymbol{n}}_P,$$
(C-3)

where $\widehat{\bar{v}}_p$, $\widehat{\varepsilon}_{kk}$ and $\widehat{\boldsymbol{n}}_P$ are the Fourier transforms of $\bar{v}_p$, ε_{kk}, and $\boldsymbol{n}_P$, i is the imaginary unit, and ω is the angular frequency. The trem $\widehat{\boldsymbol{n}}_P$ is expressed by the P-wave wavenumber vector as,

$$\widehat{\boldsymbol{n}}_P = \frac{k_P}{|k_P|}.$$
(C-4)

By substituting Equation (C-4) into Equation (C-3),

$$i\omega\bar{v}_p = \frac{\lambda + 2\mu}{\rho} (ik_x\widehat{\varepsilon}_{kk}, ik_z\widehat{\varepsilon}_{kk}) \cdot \frac{k_P}{|k_P|}.$$
(C-5)

Organizing the above equation,

$$\bar{v}_p = \frac{\lambda + 2\mu}{\rho} \cdot \frac{|k_P|}{\omega} \widehat{\varepsilon}_{kk}.$$
(C-6)

By substituting the frequency dispersion relationship $\frac{|\boldsymbol{k}_P|}{\omega} = \sqrt{\frac{\lambda + 2\mu}{\rho}}$ into Equation (C-6), and transforming it from the frequency-wavenumber domain to the time-space domain, we can obtain the scalar P-wave equation,

$$\bar{v}_p = \sqrt{\frac{\lambda + 2\mu}{\rho}} \varepsilon_{kk}.$$
(C-7)

References

Aki, K., Richards, P., 2002. Quantitative Seismology, second ed. University Science Books.

Billette, F., Brandsberg-Dahl, S., 2005. The 2004 BP Velocity Benchmark. 67th EAGE Conference & Exhibition. https://doi.org/10.3997/2214-4609-pdb.1.B035.

Birt, C., Priyambodo, D., Wolfarth, S., et al., 2020. The value of high-density blended OBN seismic for drilling and reservoir description at the Tangguh gas fields, Eastern Indonesia. Lead. Edge 39 (8), 574–582. https://doi.org/10.1190/tle39080574.1.

Chang, W.F., McMechan, G.A., 1987. Elastic reverse-time migration. Geophysics 52 (10), 1365–1375. https://doi.org/10.1190/1.1442249.

Clapp, R.G., 2008. Reverse Time Migration: Saving the Boundaries, vol. 137. Stanford Exploration Project.

Dellinger, J., Etgen, J., 1990. Wave-field separation in two-dimensional anisotropic media. Geophysics 55 (7), 914–919. https://doi.org/10.1190/1.1442906.

Du, Q., Gong, X., Zhang, M., et al., 2014. 3D PS-wave imaging with elastic reverse-time migration. Geophysics 79 (5), S173–S184. https://doi.org/10.1190/

geo2013-0253.1.

Du, Q., Zhao, Q., Li, Q., et al., 2020. A new decoupling and elastic propagator for efficient elastic reverse time migration. Geophysics 85 (5), A31–A36. https://doi.org/10.1190/geo2019-0830.1.

Du, Y., Li, E.Y., Yang, J., et al., 2019. Source-free converted-wave reverse time migration: Formulation and limitations. Geophysics 84 (1), S17–S27. https://doi.org/10.1190/geo2018-0052.1.

Duan, Y., Sava, P., 2015. Scalar imaging condition for elastic reverse time migration. Geophysics 80 (4), S127–S136. https://doi.org/10.1190/geo2014-0453.1.

Elita Li, Y., Du, Y., Yang, J., et al., 2018. Elastic reverse time migration using acoustic propagators. Geophysics 83 (5), S399–S408. https://doi.org/10.1190/geo2017-0687.1.

Fehler, M., Larner, K., 2008. SEG advanced modeling (SEAM): phase I first year update. Lead. Edge 27 (8), 1006–1007. https://doi.org/10.1190/1.2967551.

Fei, T.W., Luo, Y., Yang, J., et al., 2015. Removing false images in reverse time migration: the concept of de-primaryDe-primary reverse time migration. Geophysics 80 (6), S237–S244. https://doi.org/10.1190/geo2015-0289.1.

Granli, J.R., Arntsen, B., Sollid, A., et al., 1999. Imaging through gas-filled sediments using marine shear-wave data. Geophysics 64 (3), 668–677. https://doi.org/10.1190/1.1444576.

Graves, R.W., 1996. Simulating seismic wave propagation in 3D elastic media using staggered-grid finite differences. Bull. Seismol. Soc. Am. 86, 1091–1106. https://doi.org/10.1190/1.1442147.

Hu, T., Liu, H., Guo, X., et al., 2019. Analysis of direction-decomposed and vector-based elastic reverse time migration using the Hilbert transform. Geophysics 84 (6), S599–S617. https://doi.org/10.1190/geo2018-0324.1.

Knapp, S., Payne, N., Johns, T., 2001. Imaging through Gas Clouds: A Case History from the Gulf of Mexico. SEG Technical Program Expanded Abstracts, pp. 776–779. https://doi.org/10.1190/1.1816747.

Li, C., Huang, J.-P., Li, Z.-C., et al., 2017. Regularized least-squares migration of simultaneous-source seismic data with adaptive singular spectrum analysis. Petrol. Sci. 14 (1), 61–74. https://doi.org/10.1007/s12182-016-0134-1.

Li, J., Shen, Y., Zhang, W., 2018. Three-dimensional passive-source reverse-time migration of converted waves: the method. J. Geophys. Res. Solid Earth 123 (2), 1419–1434. https://doi.org/10.1002/2017JB014817.

Li, M., Shen, H., Guo, Y., et al., 2021. Locating microseismic events using multiplicative time reversal imaging based on decoupled wavefields in 2D VTI media: theoretical and synthetic cases studies. J. Petrol. Sci. Eng. 202 108547. https://doi.org/10.1016/j.petrol.2021.108547.

Li, Z.-C., Qu, Y.-M., 2022. Research progress on seismic imaging technology. Petrol. Sci. 19 (1), 128–146. https://doi.org/10.1016/j.petsci.2022.01.015.

Li, Z., Liu, Y., Liang, G., et al., 2021. First-order particle velocity equations of decoupled P-and S-wavefields and their application in elastic reverse time migration. Geophysics 86 (6), S387–S404. https://doi.org/10.1190/geo2020-0452.1.

Lin, Y., Zhang, H., Chen, Y., et al., 2020. Source-independent passive seismic reverse-time structure imaging with grouping imaging condition: method and application to microseismic events induced by hydraulic fracturing. J. Geophys. Res. Solid Earth 125 (2), e2019JB018043. https://doi.org/10.1029/2019JB018043.

Liu, Y., 2014. Optimal staggered-grid finite-difference schemes based on least-squares for wave equation modelling. Geophys. J. Int. 197 (2), 1033–1047 https://doi.org/1033-1047.10.1093/gji/ggu032.

Morse, P.M., Feshbach, H., 1954. Methods of Theoretical Physics. McGraw-Hill Book Company.

Qu, Y., Guan, Z., Li, Z., 2019a. Topographic elastic least-squares reverse time migration based on vector P-and S-wave equations in the curvilinear coordinates. Geophys. Prospect. 67 (5), 1271–1295. https://doi.org/10.1111/1365-2478.12775.

Qu, Y., Huang, C., Liu, C., et al., 2019b. Multiparameter least-squares reverse time migration for acoustic-elastic coupling media based on ocean bottom cable data. Appl. Geophys. 16 (3), 327–337. https://doi.org/10.1007/s11770-019-0771-4.

Qu, Y., Li, J., Huang, J., et al., 2018. Elastic least-squares reverse time migration with velocities and density perturbation. Geophys. J. Int. 212 (2), 1033–1056. https://doi.org/10.1093/gji/ggx468.

Qu, Y., Zhou, C., Liu, C., et al., 2020. P-and S-wave separated elastic reverse time migration for OBC data from fluid-solid coupled media with irregular seabed interfaces. J. Appl. Geophys. 172 103882. https://doi.org/10.1016/j.jappgeo.2019.103882.

Shabelansky, A.H., Malcolm, A.E., Fehler, M.C., et al., 2015. Source-independent full wavefield converted-phase elastic migration velocity analysis. Geophys. J. Int. 200 (2), 952–966. https://doi.org/10.1093/gji/ggu450.

Shi, Y., Zhang, W., Wang, Y., 2019. Seismic elastic RTM with vector-wavefield decomposition. J. Geophys. Eng. 16 (3), 509–524. https://doi.org/10.1093/jge/gxz023.

Stewart, R.R., Gaiser, J.E., Brown, R.J., et al., 2003. Converted-wave seismic exploration: Applications. Geophysics 68 (1), 40–57. https://doi.org/10.1190/1.1543193.

Sun, R., Chow, J., Chen, K.J., 2001. Phase correction in separating P- and S-waves in elastic data. Geophysics 66 (5), 1515–1518. https://doi.org/10.1190/1.1487097.

Sun, R., McMechan, G.A., Chuang, H.-H., 2011. Amplitude balancing in separating P- and S-waves in 2D and 3D elastic seismic data. Geophysics 76, S103–S113. https://doi.org/10.1190/1.3555529.

Sun, R., McMechan, G.A., Hsiao, H.-H., et al., 2004. Separating P- and S-waves in prestack 3D elastic seismograms using divergence and curl. Geophysics 69, 286–297. https://doi.org/10.1190/1.1649396.

Tang, C., McMechan, G.A., 2018. Multidirectional-vector-based elastic reverse time migration and angle-domain common-image gathers with approximate wavefield decomposition of P-and S-waves. Geophysics 83 (1), S57–S79. https://doi.org/10.1190/geo2017-0119.1.

Virieux, J., 1986. P-SV wave propagation in heterogeneous media: velocity-stress finite-difference method. Geophysics 51 (4), 889–901. https://doi.org/10.1190/1.1442147.

Wang, T., Cheng, J., 2015. Elastic Wave Mode Decoupling for Full Waveform Inversion. SEG Technical Program Expanded Abstracts, pp. 1461–1466. https://doi.org/10.1190/segam2015-5914394.1.

Wang, T., Cheng, J., Guo, Q., et al., 2018. Elastic wave-equation-based reflection kernel analysis and traveltime inversion using wave mode decomposition. Geophys. J. Int. 215 (1), 450–470. https://doi.org/10.1093/gji/ggy291.

Wang, W., McMechan, G.A., 2015. Vector-based elastic reverse time migration. Geophysics 80, S245–S258. https://doi.org/10.1190/geo2014-0620.1.

Wu, B., Yao, G., Cao, J.-J., et al., 2022. Huber inversion-based reverse-time migration with de-primary imaging condition and curvelet-domain sparse constraint. Petrol. Sci. https://doi.org/10.1016/j.petsci.2022.03.004.

Xiao, X., Leaney, W.S., 2010. Local vertical seismic profiling (VSP) elastic reverse-time migration and migration resolution: salt-flank imaging with transmitted P-to-S waves. Geophysics 75 (2), S35–S49. https://doi.org/10.1190/1.3309460.

Yan, J., Sava, P., 2008. Isotropic angle-domain elastic reverse-time migration. Geophysics 73 (6), S229–S239. https://doi.org/10.1190/1.2981241.

Yan, R., Xie, X.-B., 2012. An angle-domain imaging condition for elastic reverse time migration and its application to angle gather extraction. Geophysics 77, S105–S115. https://doi.org/10.1190/geo2011-0455.1.

Yang, J.-D., Huang, J.-P., Wang, X., et al., 2015. An amplitude-preserved adaptive focused beam seismic migration method. Petrol. Sci. 12 (3), 417–427. https://doi.org/10.1007/s12182-015-0044-7.

Yang, J., Zhu, H., 2019. Locating and monitoring microseismicity, hydraulic fracture and earthquake rupture using elastic time-reversal imaging. Geophys. J. Int. 216 (1), 726–744. https://doi.org/10.1093/gji/ggy460.

Yang, J., Zhu, H., Wang, W., et al., 2018. Isotropic elastic reverse time migration using the phase-and amplitude-corrected vector P-and S-wavefields. Geophysics 83 (6), S489–S503. https://doi.org/10.1190/geo2018-0023.1.

Yang, K., Dong, X., Zhang, J., 2021. Polarity-reversal correction for vector-based elastic reverse time migration. Geophysics 86 (1), S45–S58. https://doi.org/10.1190/geo2020-0033.1.

Yao, G., Wu, D., Wang, S.-X., 2020. A review on reflection-waveform inversion. Petrol. Sci. 17 (2), 334–351. https://doi.org/10.1007/s12182-020-00431-3.

Zhang, J., Tian, Z., Wang, C., 2007. P- and S-Wave Separated Elastic Wave Equation Numerical Modeling Using 2D Staggered-Grid. SEG Technical Program Expanded Abstracts, pp. 2104–2109. https://doi.org/10.1190/1.2792904.

Zhang, P., Wu, R.-S., Han, L.-G., et al., 2022. Elastic direct envelope inversion based on wave mode decomposition for multi-parameter reconstruction of strong-scattering media. Petrol. Sci. https://doi.org/10.1016/j.petsci.2022.05.007.

Zhang, R., Huang, J.-P., Zhuang, S.-B., et al., 2019. Target-oriented Gaussian beam migration using a modified ray tracing scheme. Petrol. Sci. 16 (6), 1301–1319. https://doi.org/10.1007/s12182-019-00388-y.

Zhang, W., Gao, J., Gao, Z., et al., 2020. 2D and 3D amplitude-preserving elastic reverse time migration based on the vector-decomposed P-and S-wave records. Geophys. Prospect. 68 (9), 2712–2737. https://doi.org/10.1111/1365-2478.13023.

Zhang, W., Shi, Y., 2019. Imaging conditions for elastic reverse time migration. Geophysics 84 (2), S95–S111. https://doi.org/10.1190/geo2018-0197.1.

Zhang, Y.-B., Liu, Y.-K., Yi, J., et al., 2021. First-order multiples imaging aided by water bottom. Petrol. Sci. 18 (6), 1650–1661. https://doi.org/10.1016/j.petsci.2021.09.036.

Zhao, Y., Niu, F.-L., Fu, L., et al., 2021. Local events-based fast RTM surface-offset gathers via dip-guided interpolation. Petrol. Sci. 18 (3), 773–782. https://doi.org/10.1007/s12182-021-00557-y.

Zhao, Y., Zhang, H., Yang, J., et al., 2018. Reducing artifacts of elastic reverse time migration by the deprimary technique. Geophysics 83 (6), S569–S577. https://doi.org/10.1190/geo2018-0260.1.

Zhou, X., Chang, X., Wang, Y., et al., 2018. 3D elastic reverse time migration based on P-and S-wave decoupling. Chin. J. Geophys. 61 (3), 1038–1052. https://doi.org/10.6038/cjg2018L0247.

Zhong, Y., Gu, H., Liu, Y., et al., 2021. Elastic least-squares reverse time migration based on decoupled wave equations. Geophysics 86 (6), S371–S386. https://doi.org/10.1190/geo2020-0805.1.

Zhou, X., Chang, X., Wang, Y., et al., 2019. Amplitude-preserving scalar PP and PS imaging condition for elastic reverse time migration based on a wavefield decoupling method. Geophysics 84 (3), S113–S125. https://doi.org/10.1190/geo2017-0840.1.

Zhu, H., 2017. Elastic wavefield separation based on the Helmholtz decompositionElastic wavefield separation. Geophysics 82 (2), S173–S183. https://doi.org/10.1190/geo2016-0419.1.

Zou, P., Cheng, J., 2021. Three-dimensional passive-source anisotropic reverse time migration for imaging lithospheric discontinuities. Geophys. J. Int. 226 (3), 2103–2115. https://doi.org/10.1093/gji/ggab201.